Journal of Molecular Liquids 418 (2025) 126706

Contents lists available at ScienceDirect

Journal of Molecular Liquids

journal homepage: www.elsevier.com/locate/molliq

Effect of iodides on thermal behavior and phase partitioning in LiCl-KCl

María del Rocío Rodríguez-Laguna [a,b,*], Rafael H.L. Garcia [c], Tae-Sic Yoo [a], Scott T. Anderson [d], Gregory P. Horne [e], Ruchi Gakhar [a,*]

[a] Advanced Technology of Molten Salts Department, Idaho National Laboratory, Idaho Falls, ID 83415, the United States of America
[b] Glenn T. Seaborg Institute, Idaho National Laboratory, US Department of Energy, Idaho Falls, ID 83415, the United States of America
[c] Instituto de Pesquisas Energéticas e Nucleares (IPEN/CNEN-SP), Av. Prof. Lineu Prestes, 2242, CEP 05508-000, São Paulo, SP, Brazil
[d] Irradiated Materials Characterization Laboratory, Idaho National Laboratory, Idaho Falls, ID 83415, the United States of America
[e] Center for Radiation Chemistry Research, Idaho National Laboratory, P.O. Box 1625, Idaho Falls, ID 83415, the United States of America

ARTICLE INFO

Keywords:
Molten salt
Fission product iodine
Iodide
Phase transitions
X-ray diffraction
FactSage

ABSTRACT

Liquid-fueled molten salt reactors (MSRs) are designed to operate with fissile materials and, ultimately, fission products dissolved in the primary molten salt coolant. Understanding the speciation and transport of iodine—a high-yield fission product—is essential because this element's accidental release poses significant environmental concerns due to its capacity to be readily absorbed by the human thyroid gland. Here, we report the impact of iodide species (LiI and KI) on phase transitions, phase distribution, and phase stability in LiCl–KCl-eutectic salt mixtures. The study employed a combination of computational and experimental techniques, including thermodynamic FactSage calculations, differential scanning calorimetry, and high-temperature X-ray diffraction. The results indicate that the presence of iodide (10–25 wt%) significantly alters the melting behavior of the LiCl–KCl-eutectic system. Adding 10 wt% LiI has a more-pronounced effect than 10 wt% KI, as LiI converts to KI, leading to formation of LiCl, thereby, altering the LiCl-KCl ratio which significantly affects the melting temperature of the mixture. Furthermore, the evolution of crystalline structure, solid-fraction composition, and the dynamics of mixed-halide solid–liquid partitioning as a function of temperature indicate the potential for selective iodide separation from chloride-salt mixtures via solid–liquid separation techniques. Overall, the presented findings provide valuable insights that are beneficial for the design and operation of MSRs, as well as for the safe handling and effective processing of used nuclear fuel using advanced pyrochemical techniques.

1. Introduction

The main applications of molten salts in energy technologies include power production and energy storage. Molten salt reactors (MSRs) are a key example, benefiting from molten salts' high heat capacity, low operating pressure, and ability to keep both fissile material and salt as a single-phase liquid at elevated temperatures [1]. Significant research and development on the application of molten salts in nuclear-reactor technologies, such as MSRs, was conducted during the mid-20th century, with notable experiments such as the Molten-Salt Reactor Experiment (MSRE) at Oak Ridge National Laboratory (ORNL) in the United States. For several decades, interest in MSRs waned as attention shifted to other reactor technologies. However, recent years have witnessed a renewed interest in MSR technology, with researchers exploring chloride-based salts in addition to traditional fluoride-based salts, due to their significant promise for use in fast spectrum reactors [2,3]. However, this resurgence in MSR technologies necessitates focused, multifaceted efforts to address the knowledge gaps and technical challenges to ensure safe and efficient deployment, operation, decommissioning, and waste management.

The operation of the MSRE at ORNL in the 1960s provided valuable insights, not only into the design, operation, and maintenance of an MSR, but also into the technical challenges associated with this technology. One noteworthy challenge was the production of hydrogen fluoride (HF) gas after shutdown [4]. The fuel salt experienced radiolytic decomposition during operation, leading to the generation and release of HF gas [5], which was problematic due to the corrosive nature of this compound. Salt radiolysis was also found to be exacerbated by the accumulation of fission products during operation, which altered the chemical stability of the salt mixture. In general, the fission products

* Corresponding authors at: Advanced Technology of Molten Salts Department, Idaho National Laboratory, Idaho Falls, ID 83415, the United States of America (María del Rocío Rodríguez-Laguna and Ruchi Gakhar).
E-mail addresses: rocio.rodriguez@inl.gov (M. del Rocío Rodríguez-Laguna), ruchi.gakhar@inl.gov (R. Gakhar).

https://doi.org/10.1016/j.molliq.2024.126706
Received 18 September 2024; Received in revised form 4 December 2024; Accepted 7 December 2024
Available online 9 December 2024

generated either dissolve in the molten salt coolant or precipitate out, as dictated by their inherent chemistry, the temperature of the salt, and radiation effects. Consequently, the speciation and transport of fission products are expected to have a significant impact on the fuel-salts' physical and chemical properties, both of which can impact MSR performance and longevity. The specific effects of the dynamic fuel salt composition on its melting temperature are complex and depend on the solubility and interactions between the various chemical species present. For instance, noble metal species (e.g., ruthenium, rhodium, and palladium) naturally precipitate, and even salt phases can precipitate out, forming multi-phase salt systems. This separation could have significant impacts on heat transfer and fluid dynamics within an MSR. In nuclear engineering, such effects have implications on the design and operation of a reactor, including the materials used for reactor components, the temperature at which the reactor operates, and subsequent used-fuel processing methods.

These challenges highlight the importance of addressing the chemical stability of candidate fuel salts, particularly regarding their interactions with fission products and their behavior under different thermal conditions. Current MSR-technology research has overlooked the impact of fission products on the chemical behavior, phase distribution, and phase stability of molten salts. This missing knowledge is essential for predicting and ensuring the safe operation of MSRs, especially during startup, shutdown, and accident scenarios. The knowledge gap in phase partitioning between liquid and solid salt fractions associated with fission-product accumulation is a consequence of the complexity of the chemistry involved, the difficulty in handling and analyzing highly radioactive materials, and the fact that the focus of nuclear research shifted away from MSRs for several decades after the initial MSRE. In addition, the phase behavior and partitioning between solid and liquid fractions are important factors in separating fission products for pyrochemical reprocessing and waste management. In the literature, melt-crystallization is proposed as a method to further separate fission products after pyroprocessing to reduce waste volumes [6–8]. This technique can be applied to separate fission products from used molten salts in MSRs [9]. Melt-crystallization techniques are used to separate, purify, and concentrate substances based on their melting and crystallization behavior. This process involves melting the mixture and then carefully controlling conditions to induce the desired component to crystallize out as the temperature is decreased [10]. The separation of fission products and the treatment of used fuel rely on understanding how these materials behave in the salt matrix [5]. Among all fission products, the behavior of iodine in high-temperature molten salts is a critical area of research, particularly for MSRs, where iodine can have significant impacts on both the operation and safety of the reactors and impose long-term repository challenges [11]. Iodine-129, with a half-life of 15.7 million years, is a long-lived radioisotope that raises significant concerns for long-term storage due to its potential mobility in geological repositories. Iodine-131, with a shorter half-life of 8 days, can be released into the environment during nuclear reactor operation or accidents [12–14]. Due to its volatility in these conditions [15–18], it can disperse widely through the air and can be absorbed by the thyroid gland in humans and animals, potentially causing thyroid cancer or other thyroid-related diseases [19,20]. Iodine-135 is a decay product of tellurium-135, which is a fission product of uranium-235. Iodine-135 decays into xenon-135, which is a significant neutron absorber (neutron poison) [21]. The generation and decay of xenon-135 leads to fluctuations in reactor power or even reactor shutdown if not properly managed, which was one of the factors contributing to the Chernobyl disaster [22]. Iodine exhibits complex chemistry, forming iodides at the redox potential of the fuel salt, as reported by Compere *et al.* in their analysis of the behavior of fission products in the MSRE [4]. The ORNL MSRE findings underscore a significant gap in understanding the chemical behavior of fission products, particularly iodine, as minimal iodine gas was detected in the MSRE off-gas, and up to 66 % of the generated iodine remained unaccounted for [4]. This "missing iodine" can be attributed to an absence of fundamental knowledge on its speciation under these irradiated high-temperature molten salt conditions. Considering the possible phases iodine and its precursor isotopes can be in—solid, liquid, and gas—and their transitions, which depend on chemical, thermal, and neutronics conditions, it is not surprising to encounter challenges in iodine accountancy. Consequently, it is crucial to gain a comprehensive understanding of the chemical evolution of fission-product iodine and the formation of iodide species in molten salts, which depends on the chemical state and redox potential of the salt. A better understanding of the chemical behavior of iodine in molten salts can lead to the development of more-efficient trapping and scrubbing systems for iodine capture to mitigate its release to the environment and to maintain a stable and safe reactor operation.

Understanding how the accumulation of iodine species within the salt influences its thermodynamic behavior is crucial, particularly for systems requiring a single liquid phase for purposes such as materials accountancy. However, the literature addressing this topic is notably limited. To the authors' knowledge, no studies have explicitly addressed the phase distribution and segregation of iodide species in molten chloride or fluoride salts. To address this gap, this study investigates the influence of iodide species on phase transitions and phase distribution within a chloride-salt matrix. The temperature-driven phase evolution and melting behavior of LiCl–KCl-eutectic mixture was explored in the presence of two alkali iodide solutes, lithium iodide (LiI) and potassium iodide (KI), using differential scanning calorimetry (DSC) and high-temperature X-ray diffraction (XRD) techniques. The LiCl–KCl eutectic salt system was chosen for its notable ability to dissolve fission products and its significance in the molten salt recycling process [23–26]. Moreover, the chemistry of LiCl-KCl is well characterized in terms of phase transition and phase distribution of species. This study aimed to provide insights into the complex phase distributions that arise in mixed-halide systems, particularly when iodides are introduced. To simplify a complex mixed-halide system, the cations Li^+ and K^+ were kept constant in this study. The experimental results were correlated with thermodynamic calculations to elucidate phase formation, phase-transitions temperatures, and segregation of the salts in the liquid and solid phases.

2. Methods

2.1. Salt preparation

Anhydrous KI, LiI, and LiCl–KCl-eutectic mixture of 99.99 % purity (trace-metals basis) were procured from Sigma Aldrich. The salt mixtures were prepared in glassy carbon crucibles, these were cleaned with deionized (DI) water and isopropanol (99.9 %, HPLC Plus grade, Sigma Aldrich), followed by a two-step baking process: heat inside a vacuum oven at 125 °C overnight, followed by baking at 800 °C inside an argon-atmosphere glovebox for 6 h. Samples were prepared by loading the crucibles with KI or LiI and LiCl–KCl-eutectic mixture at room temperature. Sample weights were recorded to 0.1 mg precision using a Mettler Toledo balance (model number TLE204E, tolerance 0.8 mg). The KI was evaluated at concentrations of 10 and 25 wt% while LiI was studied at 10 wt%. Total mass for each sample was approximately 5 g. The KI and LiI were held in the LiCl-KCl melt at 500 °C for 4 h to ensure complete dissolution. The compositions of the salt systems investigated by this

Table 1
Composition of samples KI-LiCl-KCl and LiI-LiCl-KCl, where the LiCl-KCl eutectic proportion was maintained (i.e., 44 wt% LiCl: 56 wt% KCl).

System	Weight %			
	KI	LiI	KCl	LiCl
10 KI	10		50.4	39.6
10 LiI		10	50.4	39.6
25 KI	25		42	33

work are shown in Table 1, including their weight percentages. From this point forward, 10 KI, 10 LiI, and 25 KI will be used to designate systems consisting of 10 wt% KI, 10 wt% LiI, and 25 wt% KI, respectively. In all systems, the LiCl–KCl-eutectic proportion was maintained, with a consistent ratio of 44 wt% LiCl to 56 wt% KCl. The iodine concentration is above what is normally expected in nuclear reactor operations. These compositions were selected based on thermodynamic calculations targeting a broad temperature range where solid and liquid phases coexist. This broad range was favorable to detect solid–liquid partitioning using XRD in this study.

2.2. Thermodynamic modeling

FactSage software, version 8.2, was employed to perform thermal-equilibrium calculations [27]. The FTsalt database, along with the equilibrium module, was used to predict the phase stability, phase transitions, and phase composition. The liquid solution FTsalt-SALTE and solid solution FTSalt-B1 were used for the presented calculations, which include the components LiCl, LiI, KCl, and KI. The reciprocal system, LiCl-KCl-LiI-KI, could not be modeled due to insufficient experimental data. Therefore, four common-ion binary subsystems were modeled (i.e., LiCl-KCl, LiI-KI, LiCl-LiI, and KCl-KI), and the predictions for these reciprocal systems were derived from model parameters obtained for the four common-ion binary subsystems. HSC Chemistry 6.0 was used to retrieve the Ellingham diagrams for LiI, KI, LiCl, and KCl, along with the temperature-dependent free energy for the reaction: $LiI + KCl \rightarrow LiCl + KI$.

2.3. Experimental techniques

DSC was employed to investigate the thermal behavior of the aforementioned salt systems by identifying phase transitions, specifically the solidus and liquidus temperatures. Calorimetric measurements were conducted using a Netzsch (Selb, Germany) simultaneous thermal analyzer (STA), model 449F3-0171-M heat-flux type calorimeter, with a type-K thermocouple embedded in the sample carrier. This equipment has the capability to perform DSC and thermogravimetric analysis (TGA) simultaneously. The STA, located inside an argon glovebox, was calibrated in temperature and energy using several standards: i.e., indium, bismuth, cesium chloride, and aluminum. These standards present clear phase transitions along the temperature range of interest, which are used for instrument calibration. For further details on the DSC calibration, refer to the *Supporting Information (SI)*. The DSC conditions involved employing ultra-high-purity argon for both the purging and protective gases, with a gas flow of 50 ml min^{-1}. Glassy carbon crucibles of 50 μl with pierced lids were used for the reference (empty crucible), calibration standards, and salt samples due to their lack of reactivity with the materials.

The determination of the onset and endset temperatures of a melting peak in DSC analysis is crucial but not straightforward. In this study, the "tangent method" was used, which involves drawing tangent lines on the baseline and peak side, at the low- and high-temperature sides of the peak to identify the onset and endset temperatures at their intersection points [28]. DSC is a dynamic technique in which the sample's temperature changes over time according to a specific scan rate (i.e., heating/cooling rate) to follow a predefined temperature program. In this type of measurement, a thermal delay between the thermocouple temperature and the actual sample temperature occurs. We are interested in determining both the solidus and liquidus temperatures. The solidus and liquidus indicate points of thermal equilibrium, defining a phase transition. The solidus temperature marks the starting point of the melting process, representing the temperature at which the material begins to form a liquid phase upon heating. On the other hand, the liquidus temperature signifies the lowest temperature at which the material is entirely in liquid phase. DSC experiments were conducted at four different scan rates: 1, 4, 7, and 10 °C min^{-1}. Following the methodology proposed by Pedersen *et al.* [29], the data points were plotted against the heating rate, fitted, and extrapolated to zero-heating rate. The extrapolated data represent the solidus estimate in the case of the onset, and the liquidus estimate in the case of the endset. A zero-heating rate approximates thermal-equilibrium conditions. The onset and endset temperatures were calculated by averaging data obtained from three heating cycles for both calibration standards and samples.

XRD measurements were performed in a Panalytical Empyrean diffractometer, equipped with a Pixel 3D detector with 0.02-mm Ni filter and high-temperature stage (Anton-Paar HTK 1200 N chamber and TCU 1000 N controller). The goniometer radius was configured to 240 mm, soller slits of 0.04 rad, anti-scatter slit of ¼ degree, and divergence slit of 0.125 degree. Scans were acquired using Cu-Kα radiation, 45 kV and 40 mA, and two-theta ranged from 5 to 80 degrees in Bragg-Brentano geometry, with step size of 0.026 degrees and 697 s per step. Scans were conducted in constant temperatures, with 10 min delay before each scan to assure thermal equilibrium and stability. The heating rate between the scans was 10 °C min^{-1}, and the cooling rate was 50 °C min^{-1}. An alumina sample holder, 0.8 mm deep with a 16 mm radius, was entirely filled with sample. The thermocouple was located underneath the alumina sample holder. The expected temperature difference between the thermocouple and sample with this configuration was ±10 °C. Chamber pressure was kept around 1×10^{-1} bar to avoid moisture because samples are hygroscopic. Phase identification was carried out in DIFFRAC.EVA software from Bruker, version 5.1, using PDF2 database from 2003.

3. Results and discussion

3.1. Experimental data

DSC was employed to determine the solidus and liquidus temperatures, as well as to study the overall thermal behavior of the systems. Fig. 1 (left) shows the DSC heating curves for system 10 KI, recorded at heating rates of 1, 4, 7 and 10 °C min^{-1}. The calorimetric curves (Fig. 1, left) illustrate endothermic peaks corresponding to the melting process of the sample. The presence of two overlapping peaks, consistently visible at different heating rates, indicates the composition is far from eutectic. The first deviation from the baseline marks the beginning of sample melting. The second peak corresponds to an additional phase transition, with the termination of this peak indicating the end of the melting process, approximating the liquidus temperature. Examining the DSC curves at different heating rates indicates that there is a thermal lag between the temperature of the DSC thermocouple and actual sample temperature. This is especially evident in the shift in the endset of the melting peak to higher temperature with increasing scan rate, as the temperature gradient across the sample is more pronounced with a faster heating rate. This shows that determining the liquidus temperature using a high heating rate, such as 10 °C min^{-1}, can lead to overestimation, even when using peak values. To identify the solidus and liquidus temperatures, we plot the peak onset and endset data against the heating rate and extrapolate to a heating rate of zero, as illustrated in Fig. 1 (right). The error bars represent twice the standard deviation of the measured values from three DSC runs per heating rate. This zero-heating-rate approximation proposed by Pedersen *et al.* [29] represents thermal-equilibrium conditions, thereby providing temperature values closer to the actual solidus and liquidus temperatures. The DSC curves in Fig. 1 (left) display raw data and are not temperature calibrated. The temperature-calibration curve was generated by plotting the theoretical transition temperatures of the standards against the experimental temperatures of the standards at zero heating rate (for further details, refer to the SI). Applying this calibration curve to the provided y-intercepts from Fig. 1 (right), the zero-heating-rate temperatures were corrected to account for instrument inaccuracies. The solidus and liquidus experimental temperatures (extrapolated to zero-heating rate and DSC temperature corrected values) are denoted by black and blue lines

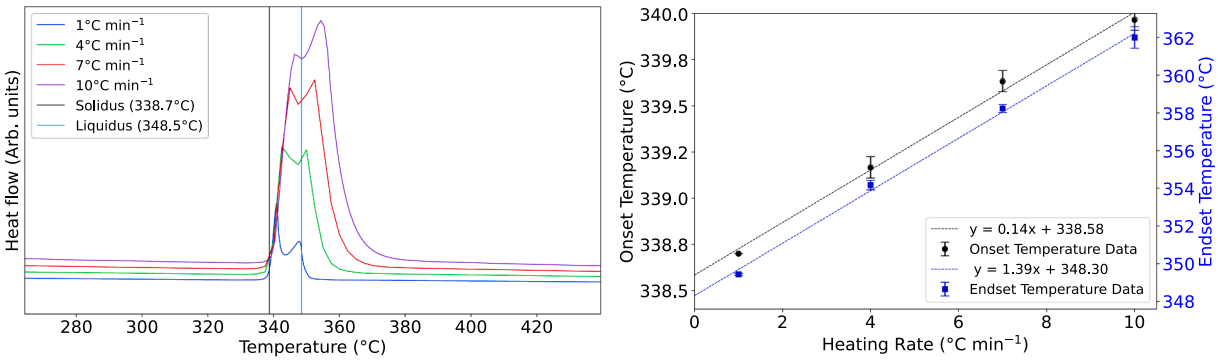

Fig. 1. (Left) DSC heating curves (endo up) corresponding to system 10 KI, conducted at heating rates of 1 (blue), 4 (green), 7 (red) and 10 °C min^{-1}(purple). (right) Average onset (black) and endset (blue) values of the melting peak of the system 10 KI as a function of heating rate.

in Fig. 1 (left), at 338.7 and 348.5 °C, respectively. Hereafter, when discussing the experimental solidus and liquidus temperatures, the temperature-corrected onset and endset values of the melting peak at zero-heating rate will be used.

Fig. 2 shows the diffractograms of system 10 KI at different temperatures. At room temperature, 25 °C, four different phases are observed, including three face-centered cubic phases (Fm-3 m): potassium chloride (PDF 41-1476), lithium chloride (PDF 04-0664), and potassium iodide (PDF 04-0471). The fourth phase present is tetragonal (P42/nmc) lithium chloride hydrate (PDF 73-1273). This hydrated form likely resulted from brief air exposure during the transfer of the sample from the vial to the XRD sample holder. The lithium chloride-hydrate peak disappeared at higher temperatures. The peaks corresponding to the cubic lithium chloride phase were observed at angles consistent with the pure compound. However, peaks for potassium chloride and potassium iodide showed shifts compared to their respective patterns available in the PDF database. This can be attributed to the ion substitution occurring within the atomic position of the crystalline phases. In other words, the expansion of the KCl cell might be due to the partial substitution of Cl^- by I^-. Similarly, the contraction of the KI cell might be attributed to the partial substitution of I^- by Cl^- in the structure. Vegard's law [30] was used to estimate the composition of these solid solutions (refer to Section 3.2 for further details). Peaks related to LiI were not identified. Additionally, a shift of all peaks to lower 2-theta angles was noted at higher temperatures, indicative of thermal expansion of the crystal lattices. Comparing the diffractograms at different temperatures reveals a noticeable change in the diffraction pattern between 330 and 340 °C, with KI peaks no longer visible, indicating the solidus transition. This observation aligns with the solidus temperature determined via DSC (338.7 °C). The diffractograms show that KCl phase melts around 345 °C while LiCl phase remains as the sole component of the solid phase. The absence of LiCl phase at 350 °C is evident, indicating that the sample is completely molten. This result is consistent with the DSC data, where the experimental liquidus temperature was determined to be 348.5 °C. It is important to note that the XRD experiment was conducted under thermal-equilibrium conditions.

The absence of KI peaks above the solidus temperature could be attributed to the phase concentration being well below the detection limits of the X-ray diffractometer. Furthermore, it is important to note that above the solidus temperature, both solid and liquid phases coexist, with solid particles floating in the liquid. This can prevent the solid particles from achieving the proper orientation of their crystal planes for

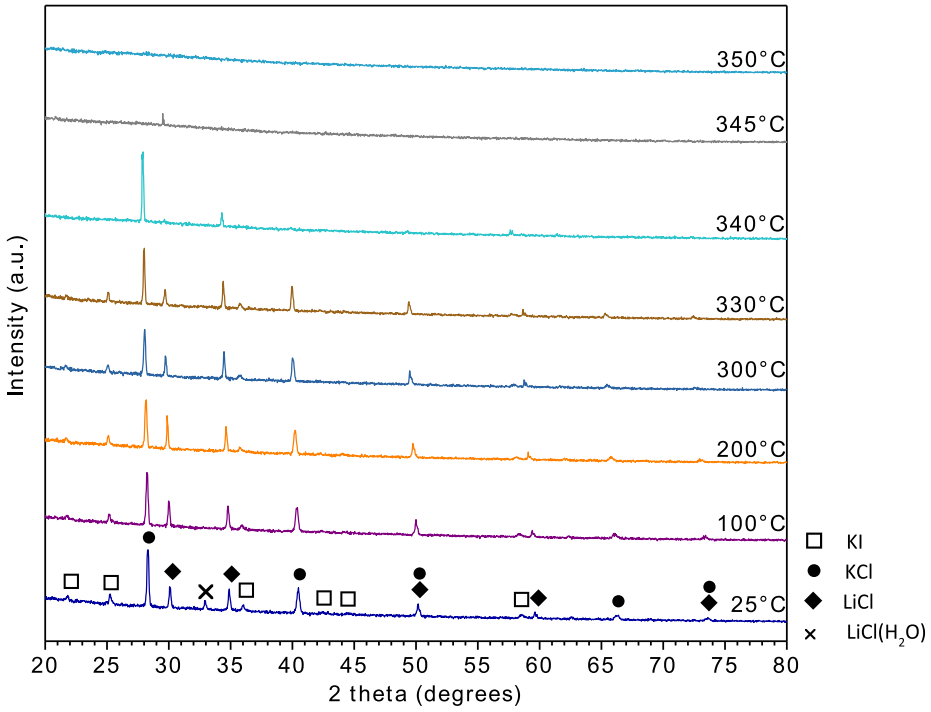

Fig. 2. X-ray diffractograms of 10 KI system analyzed from 25–350 °C.

diffraction during XRD analysis. Rietveld refinement was performed as a quantitative method to track the evolution of the solid fraction composition of system 10 KI with temperature. For detailed information, please refer to the SI.

In summary, the melting temperature of system 10 KI, with a liquidus temperature of 348.5 °C, is comparable to that of the eutectic LiCl-KCl, which has a melting point of 352 °C. This means that the presence of 10 wt% of KI does not affect the melting behavior of the LiCl-KCl system significantly. Furthermore, it was discovered that unlike LiCl, both KI and KCl tend to form solid solutions. Because all the species transition to the liquid phase sequentially within a narrow temperature range (338.7–348.5°C, according to DSC) in this system, separating any of the species using melt-crystallization would be challenging.

Fig. 3 (left) shows the DSC heating curves for system 10 LiI, recorded at heating rates of 1, 4, 7, and 10 °C min^{-1}. The calorimetric curves illustrate endothermic peaks corresponding to the melting process of the sample. The observed endothermic peak is complex, consisting of two overlapping peaks and a broad shoulder on the right side of the melting peak. The first peak corresponds to the solidus transition. The second peak is clearly visible at a 1 °C min^{-1} heating rate, where peak resolution improves noticeably compared to the 10 °C min^{-1} scan. This second peak corresponds to an additional phase transition while the broad shoulder that returns to the baseline indicates the end of the melting process (liquidus transition). Fig. 3 (right) shows the onset and endset data of the complex melting peak plotted as a function of heating rate, displaying the linear equations and the y-intercepts at heating rate = 0 °C min^{-1}. The extrapolated values to zero-heating rate, 338.4 and 390.2 °C (DSC uncorrected), estimate the solidus and liquidus temperatures, respectively. The DSC corrected values are 338.5 and 390.7 °C, respectively. It is noteworthy that the addition of 10 wt% of LiI to LiCl-KCl significantly increases the melting temperature of the system, to 390.2 °C, compared to the LiCl-KCl eutectic melting at 352 °C.

Fig. 4 shows the diffractograms of system 10 LiI at different temperatures. At an ambient temperature of 25 °C, three different phases are observed, including three face-centered cubic phases (Fm-3 m): potassium chloride (PDF 41-1476), lithium chloride (PDF 04-0664), and potassium iodide (PDF 04-0471). Peaks related to LiI were not identified, even though it was used as a starting reactant. Li^{+} recombines with Cl^{-} due to its higher stability and, in turn, KI is formed.

Fig. 5 (left) presents an Ellingham diagram, a valuable tool for comparing the stability of different compounds at various temperatures. This diagram plots the Gibbs free energy of formation (ΔG) versus temperature for multiple species, providing a clear visual representation of their relative stabilities. The Ellingham diagram for LiI, KI, LiCl, and KCl, generated using HSC Chemistry 6, shows how their stability changes with temperature. Lower ΔG values on the diagram indicate greater stability. Therefore, the species with the lowest line (i.e., the most-negative ΔG values) at a given temperature is the most stable.

Equilibrium composition can be assessed by examining a plot of ΔG versus temperature to understand the thermodynamic favorability of reactions, as shown in Fig. 5 (right). Negative ΔG values indicate that the reaction will proceed spontaneously. The formation of LiCl and KI consistently shows more-negative ΔG values upon reaction of LiI and KCl across all temperatures examined, meaning that the formation of KI is preferred over LiI at any given temperature under the same conditions.

The formation of KI and LiCl alters the proportion LiCl-KCl (pseudo-binary eutectic proportion) leading to divergence in the composition of the reciprocal system (LiI-KI-KCl-LiCl), resulting in higher liquidus temperature and a lingering solid phase at higher temperatures, as shown in Fig. 4 (350–375 °C scans). Assuming all LiI is converted to KI, the 10 LiI system would change to a composition of 12.4 wt% KI, 44.8 wt % KCl, and 42.8 wt% LiCl.

Similar to 10 KI system, XRD analysis at 25 °C for 10 LiI (Fig. 4) shows that peaks for the LiCl phase matched angles typical of the pure compound, while peaks for KCl and KI exhibited shifts from the reference patterns in the PDF database. Between 345 and 350 °C, the diffraction pattern changes, with KI and KCl peaks being no longer visible, indicating the solidus transition. This behavior aligns with the solidus temperature determined via DSC (i.e., 338.5 °C). Above 350 °C, LiCl phase is the sole component in the solid fraction. The LiCl phase remains present up to 375 °C. The diffractogram recorded at 400 °C shows imperceptible LiCl peaks, indicating that this temperature is close to the liquidus transition. This result is consistent with the DSC data by which the experimental liquidus temperature was determined to be 390.7 °C. Rietveld refinement was performed as a quantitative method to track the evolution of the solid fraction composition of system 10 LiI with temperature. For detailed information, please refer to the SI.

Combined with XRD, DSC helps identify which species are soluble in the liquid fraction. For system 10 LiI, DSC shows a broad shoulder at the end of the peak, and XRD indicates that the solid phase at these temperatures is primarily LiCl. This suggests that LiCl concentration is beyond the solubility limit in the liquid around 350–390 °C, requiring a higher temperature to fully dissolve.

To summarize, in contrast to 10 wt% KI system, the presence of 10 wt % LiI has a pronounced impact on the melting behavior of the system. While the LiCl-KCl eutectic melts at 352 °C, the 10 LiI system has an elevated liquidus temperature of 390.7 °C, which is attributed to the conversion of LiI to KI and LiCl. The diffraction patterns at different temperatures provide indirect information on the solidus and liquidus temperatures. It can be observed that the solidus and liquidus temperatures determined via XRD agree with the DSC values within ±10 °C. This discrepancy is within the expected range, based on tests conducted in the XRD furnace to determine the temperature difference between the thermocouple and sample locations. XRD results show that LiCl is the sole component of the solid fraction within an extended temperature range, which means that it would be possible to separate part of LiCl from KI and KCl by melt-crystallization.

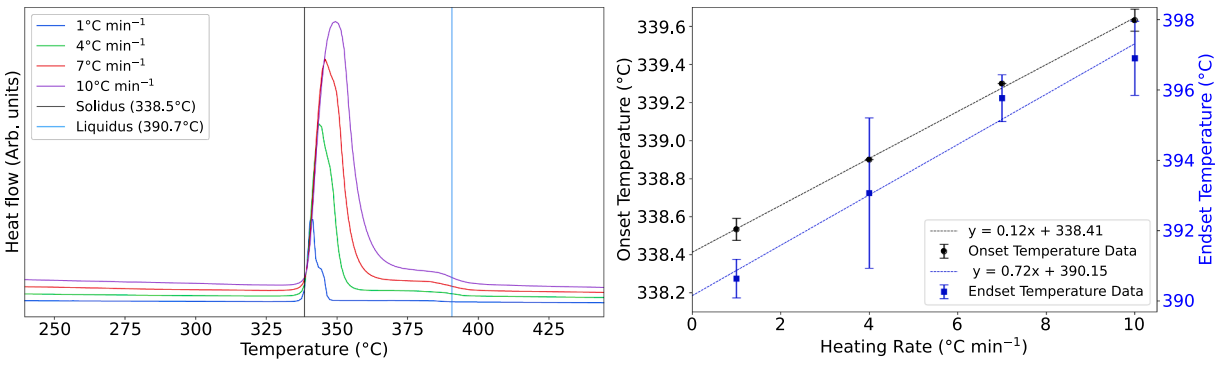

Fig. 3. (Left) DSC heating curves (endo up) of system 10 LiI at 1 (blue), 4 (green), 7 (red), and 10 °C min^{-1} (purple). (right) Average onset (black) and endset (blue) values of the melting peak of the system 10 LiI as a function of heating rate.

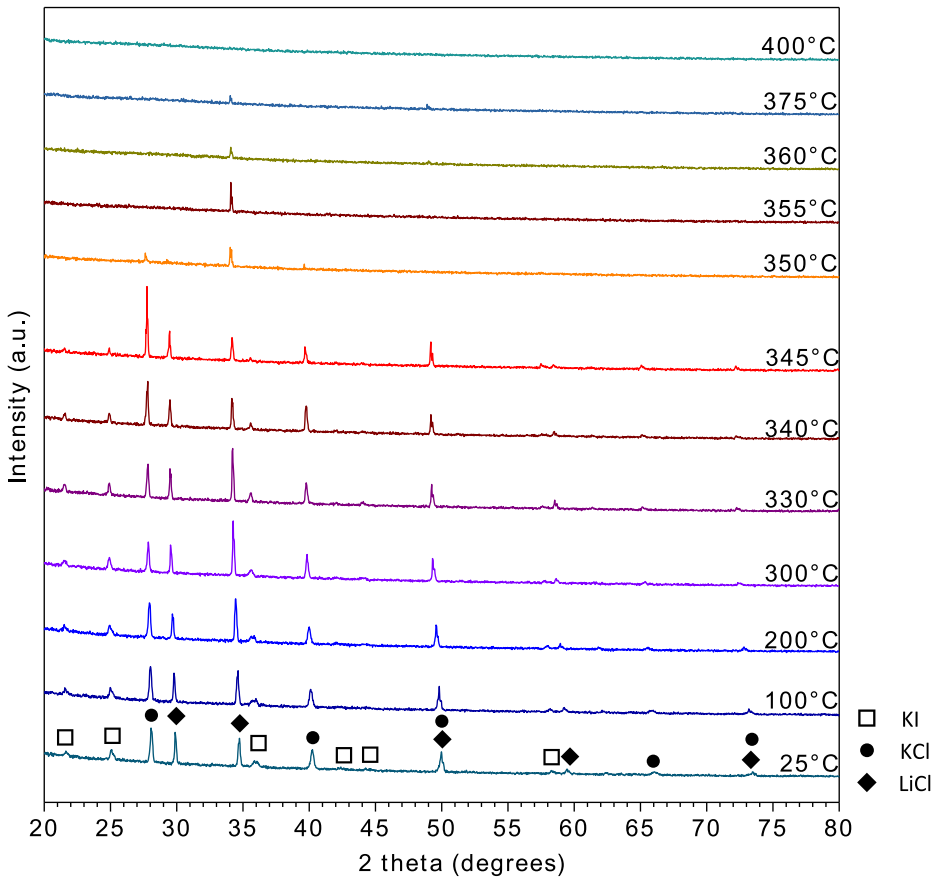

Fig. 4. X-ray diffractograms of 10 LiI sample analyzed from 25–425 °C.

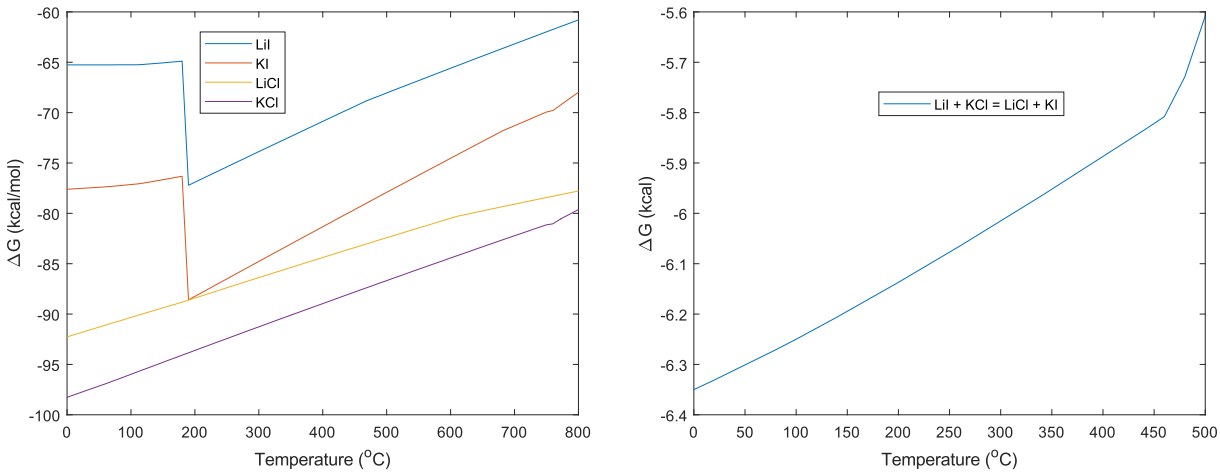

Fig. 5. (Left) Ellingham diagram of LiI, KI, LiCl, and KCl. Lower ΔG values indicate greater stability of the species. (right) ΔG vs. Temperature plot for 'LiI + KCl → LiCl + KI' reaction. Negative ΔG values indicate the preferential formation of KI over LiI. For all temperatures examined, the formation of KI is favored over LiI.

Fig. 6 (left) shows the DSC heating curves for system 25 KI, recorded at heating rates of 1, 4, 7 and 10 °C min^{-1}. The calorimetric curves (Fig. 6, left) illustrate an endothermic peak corresponding to the melting of the sample. An endothermic peak is observed, with a main peak and a broad shoulder on its right side. Fig. 6 (right) shows the onset and endset data of the complex melting peak plotted as a function of heating rate, displaying the linear equations and the y-intercepts at heating rate = 0 °C min^{-1}. The extrapolated values to zero-heating rate, 338.4 and 371.7 °C, approximate the solidus and liquidus temperatures, respectively. The DSC corrected values are 338.5 and 372.1 °C, respectively. The endset datapoint at 10 °C min^{-1} is considered an outlier (Fig. 6, right). At lower heating rates, the DSC curves exhibit a broad shoulder on the right side of the peak, indicating that the material has not melted completely (Fig. 6, right). This shoulder is absent in the 10 °C min^{-1} curve, due to the rapid heating rate preventing the material from reaching thermal equilibrium. According to DSC, the addition of 25 wt% of KI to LiCl-KCl increases the melting temperature of the system to 372.1 °C, compared to the LiCl-KCl eutectic melting at 352 °C.

Fig. 7 shows a series of diffractograms recorded at temperatures between 25 and 400 °C for 25 KI. XRD analysis at 25 °C reveals the

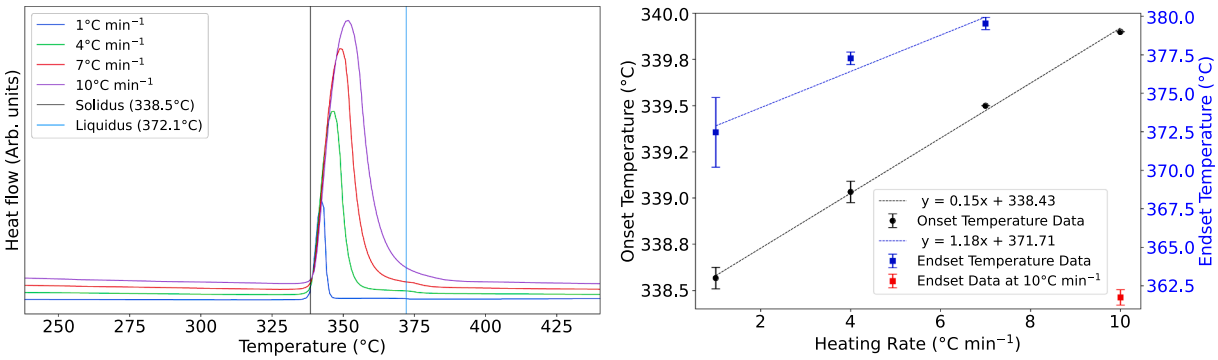

Fig. 6. (Left) DSC heating curves (endo up) corresponding to system 25 KI, conducted at heating rates of 1 (blue), 4 (green), 7 (red) and 10 °C min^{-1} (purple). (right) Average onset (black) and endset (blue) values of the melting peak of the system 25 KI as a function of heating rate.

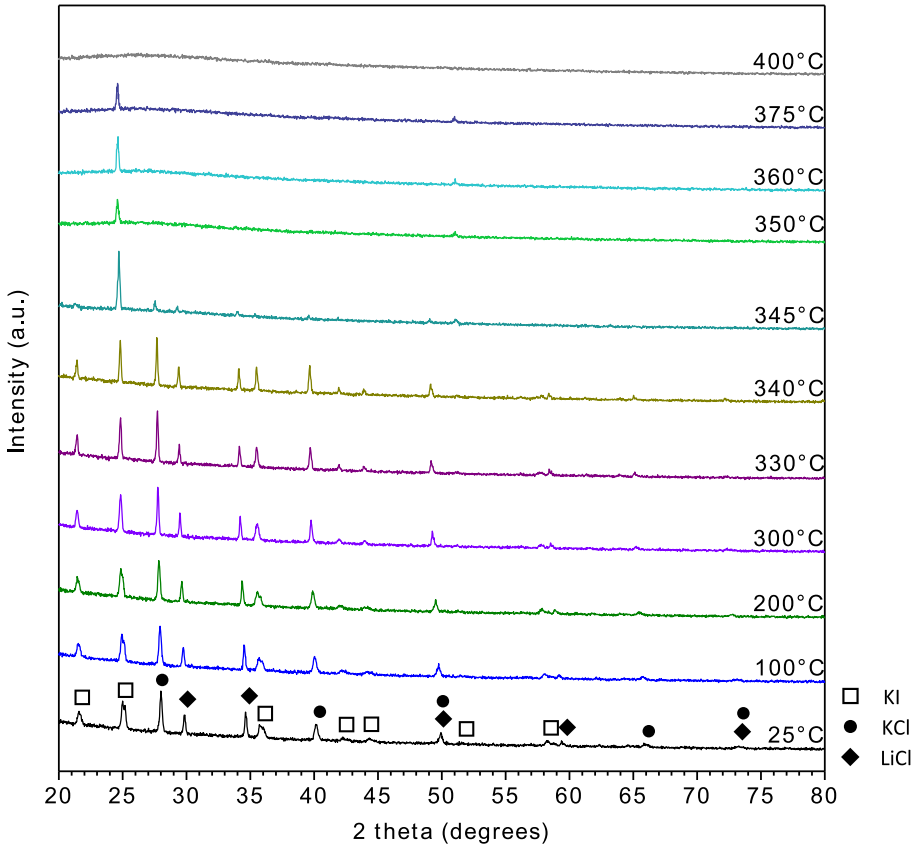

Fig. 7. X-ray diffractograms of 25 KI sample analyzed from 25–400 °C.

presence of three different phases, including three face-centered cubic phases (*Fm*-3*m*): KCl (PDF 41-1476), LiCl (PDF 04-0664), and KI (PDF 04-0471). The LiCl phase matched angles typical of the pure compound while peaks for KCl and KI exhibited shifts from their expected patterns in the PDF database. This indicates that KI forms a solid solution with KCl ($KI_{1-x}Cl_x$) and vice versa ($KCl_{1-x}I_x$), where x represents the mole fraction of substituting ions. Between 340 and 345 °C, the diffraction pattern changes, and LiCl and KCl peaks' intensity decrease until they are no longer visible, indicating the solidus transition is taking place. This result aligns with the solidus temperature value determined via DSC (338.5 °C). From 350 to 375 °C, KI is the only phase present in the solid fraction. Compared to the results from system 10 KI, where chloride species were the predominant solid phases at higher temperatures, increasing the KI concentration to 25 wt% results in KI's becoming the dominant solid phase. At 400 °C, no diffraction peak is observed, indicating that the sample is completely amorphous. According to XRD, the liquidus temperature must lie between 375 and 400 °C. This result is consistent with DSC data, where the experimental liquidus temperature was determined to be 372.1 °C. Rietveld refinement was performed as a quantitative method to track the evolution of the solid fraction composition of system 25 KI with temperature. For detailed information, please refer to the SI.

For system 25 KI, DSC shows a broad shoulder at the end of the peak, and XRD indicates that the solid phase at these temperatures is primarily KI. This suggests that KI concentration is beyond the solubility limit in the liquid at around 350–372.05 °C, requiring a higher temperature to fully dissolve.

In summary, the presence of 25 wt% KI in the LiCl-KCl system considerably affects the mixture's melting temperature. The 25 KI system has a liquidus temperature of 372.1 °C whereas LiCl–KCl-eutectic

melts at 352 °C. However, the presence of 25 wt% KI does not affect the melting behavior as significantly as 10 wt% of LiI. In systems with multiple anions and cations, the melting behavior is contingent upon the specific cations present and their interaction with the anions, which in turn affects the stability of the phases and thermal behavior. Such systems are more complex than single-anion systems. Both DSC and XRD provided consistent data on the solidus and liquidus temperatures. XRD results show that KI is the sole component of the solid fraction within an extended temperature range, which means that it would be feasible to separate part of KI from LiCl and KCl by melt-crystallization.

Table 2 summarizes the results on the experimental solidus and liquidus temperatures of KI and LiI systems determined using DSC by extrapolating to zero heating rate. These temperatures are corrected for DSC, with the associated error accounting for the standard deviation of the measured samples (three measurements per sample and heating rate) and the standard deviation from the calibration curve.

3.2. Modeled data

Thermodynamic calculations were performed using FactSage software to determine the phase transitions and identify the phases present in the systems.

Table 3 displays the phase-transition temperatures for systems 10 KI, 10 LiI, and 25 KI determined using FactSage Equilibrium module with the FTSalt database. All three compositions exhibit a solid-to-solid transition, along with solidus and liquidus transitions, and an additional transition occurring between the solidus and liquidus. Table 4 compares the modeled data for solidus and liquidus temperatures with experimentally determined values. The solid-to-solid transitions predicted by the calculations for the three compositions were not observed with DSC. This could be because the transition involves a small amount of heat that is difficult for the DSC to detect, or it could be attributed to an inaccurate prediction by the software.

Phase transitions 2 and 4 correspond to the solidus and liquidus, respectively (Table 3). The modeled solidus temperatures are similar for 10 KI, 10 LiI, and 25 KI, with values around 345–346 °C. In contrast, the DSC data show a consistent solidus temperature with an average of 338.6 ± 0.09 °C for all three systems. This is likely the eutectic temperature of the reciprocal system KI-LiI-KCl-LiCl.

Based on the calculations, the addition of 10 wt% of either KI or LiI leads to a rise in the melting temperature (see modeled liquidus) of approximately 15–20 °C relative to the binary eutectic LiCl-KCl, melting at 352 °C. On the other hand, the addition of 25 wt% KI results in an increase in the melting temperature by almost 30 °C. It is important to note that the modeled liquidus temperatures for 10 KI and 10 LiI are very similar. Hence, the calculations predict that adding 10 wt% of either KI or LiI to LiCl-KCl will affect the melting behavior similarly. This observation does not align with the DSC values obtained for the liquidus temperature of these two systems. Table 4 illustrates the disparities between the modeled and experimentally determined solidus and liquidus temperatures. FactSage underestimated the liquidus temperature for 10 LiI, indicating a smaller impact when adding LiI to LiCl-KCl. On the other hand, FactSage overestimated the effect of adding 10 wt% KI to LiCl-KCl. The DSC-measured liquidus temperature of the system with 10 wt% KI showed a slight decrease compared to the binary eutectic LiCl-KCl. The modeled liquidus temperature for 25 KI closely approximates the DSC-measured value.

Table 2
Experimental solidus and liquidus temperatures of the systems, determined using DSC by extrapolating to zero heating rate. DSC corrected temperatures.

System	Solidus temperature (°C)	Liquidus temperature (°C)
LiCl-KCl (eutectic)	352*	352*
10 KI	338.69 ± 0.01	348.48 ± 0.05
10 LiI	338.52 ± 0.01	390.66 ± 0.08
25 KI	338.54 ± 0.01	372.05 ± 1.27

* Data obtained from FactSage software and FTSalt database.

Table 3
Phase transitions for systems 10 KI, 10 LiI, and 25 KI according to FactSage calculations (Equilibrium module, FTSalt database).

Transitions	1	2	3	4
Type	solid–solid	solid–liquid (solidus)	solid–liquid	solid–liquid (liquidus)
10 KI	288.5 °C	346 °C	348.3 °C	372 °C
10 LiI	333.3 °C	345 °C	347.1 °C	368.3 °C
25 KI	146.4 °C	344.8 °C	375.3 °C	378.8 °C

Table 4
Modeled and experimentally determined solidus and liquidus temperatures for system 10 KI, 10 LiI, and 25 KI.

System	Solidus temperature (°C)		Liquidus temperature (°C)	
	DSC	FactSage	DSC	FactSage
10 KI	338.69 ± 0.01	346	348.48 ± 0.05	372
10 LiI	338.52 ± 0.01	345	390.66 ± 0.08	368.3
25 KI	338.54 ± 0.01	344.8	372.05 ± 1.27	378.8

The calculations also indicate the presence of an additional phase transition between the solidus and liquidus, occurring at 348.3, 347.1, and 375.3 °C for 10 KI, 10 LiI, and 25 KI systems, respectively (Table 3). This information aligns with the behavior observed in the DSC curves. Fig. 1 (left) and Fig. 3 (left) show the DSC curves for 10 KI and 10 LiI, respectively. When analyzing the DSC curves for 10 KI and 10 LiI at 1 °C min^{-1}, a double peak is evident. The second peak corresponds to an additional solid-to-liquid transition occurring around 347 °C for 10 KI (just below the liquidus transition) and approximately 345 °C for 10 LiI. These values align closely with the modeled temperatures for this additional transition. In the case of the DSC curves for 25 KI, Fig. 7 (left), a broad shoulder is observed that does not precisely correspond with the modeled additional solid-to-liquid transition temperature.

The discrepancies between the calculated and experimental data can be attributed to the fact that the reciprocal LiCl-KCl-LiI-KI system has not been completely evaluated due to insufficient experimental data. Predictions for the reciprocal system are derived from model parameters obtained for the four binary common-ion subsystems (KI-LiI, LiI-LiCl, KCl-LiCl, and KCl-KI). This highlights the importance of studying and characterizing pseudo-binary and ternary systems to accurately predict and understand higher-order systems, especially in reciprocal systems.

Thermodynamic calculations were conducted to identify the phases present in the systems. The calculations reveal the presence of rock-salt structures. Chloride and iodide crystals commonly exhibit a halide or rock-salt (cubic) structure. Consequently, in the solid region, the prevailing phases are characterized by rock-salts designated by FactSage software as #1, #2, and #3. Rock-salt #1 is composed of pure LiCl. Rock-salt #2 is a structure primarily composed of KCl-sylvite with a presence of KI whereas rock-salt #3 contains KI as the major component with KCl-sylvite present. The calculations indicate the presence of these three rock-salts in all three systems—i.e., 10 KI, 10 LiI, and 25 KI. According to the calculations, KI: KCl proportion changes with temperature in the solid solutions. The absence of LiI as a component in any of the rock-salts is noticeable, despite LiI being included as part of system 10 LiI in the calculations. This result is consistent with the experimental XRD data, which show that the LiI diffraction pattern is not present in the diffractograms.

Rietveld refinements of the XRD data revealed a shift of KCl and KI peaks at room temperature. As mentioned previously, this can be attributed to the ion substitution in atomic position within crystalline phases. LiCl peaks did not exhibit relevant lattice parameter variation. These results agree with the calculations, which predict solid solutions of $KI_{1-x}Cl_x$ and $KCl_{1-x}I_x$. Table 5 shows the experimentally determined

Table 5
XRD and FactSage modeled data composition of $KCl_{1-x}I_x$ and $KI_{1-x}Cl_x$ solid solutions, with I and Cl proportions given in at. %, for 10 LiI, 10 KI, and 25 KI samples at 25 °C, as estimated from Vegard's law and FactSage, respectively.

XRD data					Modeled data (FactSage)	
Sample	Phase	Lattice parameter (Å)	%I	%Cl	%I	%Cl
Standard (PDF)	KI	7.066	100.0	0.0		
Standard (PDF)	KCl	6.292	0.0	100		
10 KI	KI	7.046	96.3	3.7	98.4	1.6
10 KI	KCl	6.296	0.2	99.8	0.1	99.9
10 LiI	KI	7.056	98.1	1.9	98.4	1.6
10 LiI	KCl	6.306	0.9	99.1	0.1	99.9
25 KI	KI	7.030	93.5	6.5	100	0
25 KI	KCl	6.308	1.0	99.0	0.1	99.9

and modeled composition of KI and KCl phases for 10 KI, 10 LiI, and 25 KI systems.

According to Vegard's law [30], it is possible to estimate the composition of each phase according to its lattice parameters. However, for better accuracy, it is important to use a correlation based on standards because the variation of the lattice parameters is not linearly related to the concentration of a certain ion in the structure. Fortunately, Amrani *et al.* [31], from a first-principles study, determined the shape of the Vegard's law for the KCl-KI system. This curve was adjusted to match the values of lattice parameters of pure KCl and KI that were used as references in this work (from PDF files) and the results are shown in Table 5. LiCl was not used in these calculations because it did not exhibit relevant lattice-parameter variation.

Table 5 shows that the composition of the $KCl_{1-x}I_x$ solid solution determined via XRD and FactSage matches reasonably well for all three systems. In contrast, the modeled composition of the $KI_{1-x}Cl_x$ solid solution differs slightly from the experimental data across all three systems. In the experimental data, the $KI_{1-x}Cl_x$ solid solution exhibits a higher concentration of Cl^- compared to the modeled data.

4. Conclusions

The addition of alkali iodides (LiI and KI) to LiCl-KCl eutectic salt significantly alters its melting behavior, with 10 wt% LiI having a more pronounced effect than 10 wt% KI. This behavior is due to the complete conversion of LiI to KI, the subsequent formation of LiCl alters the LiCl-KCl ratio. This deviation from the eutectic ratio of LiCl-KCl increases the melting temperature of the reciprocal system. This study reveals how the interplay between iodide chemistry and different metal cations affect the thermodynamic properties and phase behavior of the base salt, providing valuable insights for applications in MSRs and the pyrochemical processing of used fuel salt. The observed discrepancies between experimental data and model predictions underscore the need for more-comprehensive models, particularly for mixed-halide systems, where differences between experiment and calculations are notable. Future research will focus on refining these models and exploring the separation potential of other iodide-containing systems. This will provide valuable insights into species separation for practical applications. These findings pave the way for improved design and optimization of molten salt systems, contributing to safer and more-efficient nuclear technologies.

CRediT authorship contribution statement

María del Rocío Rodríguez-Laguna: Writing – original draft, Visualization, Project administration, Methodology, Investigation, Formal analysis, Data curation. **Rafael H.L. Garcia:** Writing – review & editing, Visualization, Formal analysis. **Tae-Sic Yoo:** Writing – review & editing, Visualization, Formal analysis. **Scott T. Anderson:** Investigation. **Gregory P. Horne:** Writing – review & editing, Project administration, Funding acquisition. **Ruchi Gakhar:** Writing – original draft, Resources, Project administration, Methodology, Funding acquisition, Conceptualization.

Declaration of competing interest

The authors declare that they have no known competing financial interests or personal relationships that could have appeared to influence the work reported in this paper.

Acknowledgements

This work was supported by the U.S. Department of Energy (US-DOE), Office of Science, Basic Energy Sciences through the Chemical and Materials Sciences to Advance Clean Energy Technologies and Low-Carbon Manufacturing initiative under contract DE-AC07-05ID14517 at INL.

Appendix A. Supplementary data

Supplementary data to this article can be found online at https://doi.org/10.1016/j.molliq.2024.126706.

Data availability

Data will be made available on request.

References

[1] A. Ho, M. Memmott, J. Hedengren, K.M. Powell, Exploring the benefits of molten salt reactors: An analysis of flexibility and safety features using dynamic simulation, Digit. Chem. Eng. 7 (2023) 100091, https://doi.org/10.1016/j.dche.2023.100091.
[2] R. Gakhar, W.C. Phillips, G. Cao, T.-S. Yoo, M.E. Woods, G.L. Fredrickson, T. Karlsson, Molten salt fuels: properties, purification, and corrosion control, Encycl. Nucl. Energy 2 (2021) 366–376, https://doi.org/10.1016/b978-0-12-819725-7.00191-4.
[3] M. Aghili Nasr, A. Zolfaghari, R. Akbari, A. Cammi, S. Amirkhosravi, Neutronic and fuel cycle performance analysis of fluoride and chloride fuels in Molten Salt Fast Reactor (MSFR), Nucl. Eng. Des. 413 (2023), https://doi.org/10.1016/j.nucengdes.2023.112506.
[4] E.L. Compere, S.S. Kirslis, E.G. Bohlmann, F.F. Blankenship, W.R. Grimes, Fission product behavior in the Molten Salt Reactor Experiment, Oak Ridge, TN (United States), 1975. Doi: 10.2172/4077644.
[5] W.R. Grimes, Chemical Research and Development for Molten-Salt Breeder Reactors. Oak Ridge, TN (United States), 1967. Doi: 10.2172/4355677.
[6] M. Shim, H.G. Choi, K.W. Yi, I.S. Hwang, J.H. Lee, Separation of CsCl and $SrCl_2$ from a ternary CsCl-$SrCl_2$-LiCl via a zone refining process for waste salt minimization of pyroprocessing, J. Nucl. Mater. 480 (2016) 403–410, https://doi.org/10.1016/j.jnucmat.2016.09.003.
[7] A.N. Williams, M. Pack, S. Phongikaroon, separation of strontium and cesium from ternary and quaternary lithium chloride-potassium chloride salts via melt crystallization, Nucl. Eng. Technol. 47 (2015) 867–874, https://doi.org/10.1016/j.net.2015.08.006.
[8] Y.-Z. Cho, G.-H. Park, H.-S. Lee, I.-T. Kim, D.-S. Han, Concentration of cesium and strontium elements involved in a LiCl waste salt by a melt crystallization process, Nucl. Technol. 171 (2010) 325–334, https://doi.org/10.13182/NT09-7.
[9] M. del R. Rodríguez-Laguna, K.R. Tolman, M.T. Kropp, J.A. Yingling, S. Castro Baldivieso, T. Yoo, Separation of fission products from high-level waste salt systems by partial crystallization: CsCl-NaCl-LiCl-KCl study, Sep. Purif. Technol. 332 (2024) 125602, https://doi.org/10.1016/j.seppur.2023.125602.
[10] J.R. Versey, S. Phongikaroon, M.F. Simpson, Separation OF CsCl from LiCl-CsCl molten salt by cold finger melt crystallization, Nucl. Eng. Technol. 46 (2014) 395–406, https://doi.org/10.5516/NET.06.2013.082.
[11] R.M. Bartholomew, F. Brown, R.C. Hawkings, W.F. Merritt, L. Yaffe, The fission yield of I^{131} in the thermal neutron fission of U^{235}, Can. J. Chem. 31 (1953) 120–125, https://doi.org/10.1139/v53-016.
[12] J.W. Poston, Iodine-129: a review of its potential impact on the environment, Oak Ridge, TN (United States), 1978. Doi: 10.2172/6708312.
[13] X. Hou, V. Hansen, A. Aldahan, G. Possnert, O.C. Lind, G. Lujaniene, A review on speciation of iodine-129 in the environmental and biological samples, Anal. Chim. Acta. 632 (2009) 181–196, https://doi.org/10.1016/j.aca.2008.11.013.

[14] D.D. Ulmer, L.B. Perkins, J.G. Kereiakes, Alterations in iodine-131 distribution in the rat after whole-body X-irradiation, Radiat. Res. 11 (1959) 810, https://doi.org/10.2307/3570720.
[15] M. Taira, Y. Arita, M. Yamawaki, The evaporation behavior of volatile fission products in FLiNaK salt, Open Access J. Sci. Technol. 05 (2017), https://doi.org/10.11131/2017/101315.
[16] Y. Sekiguchi, K. Uozumi, T. Koyama, T. Terai, Fundamental study on the vaporization of cesium and iodine dissolved in LiF-NaF-KF molten salt, J. Nucl. Mater. 522 (2019) 136–143, https://doi.org/10.1016/j.jnucmat.2019.05.014.
[17] J. Kalilainen, S. Nichenko, J. Krepel, Evaporation of materials from the molten salt reactor fuel under elevated temperatures, J. Nucl. Mater. 533 (2020) 152134, https://doi.org/10.1016/j.jnucmat.2020.152134.
[18] O. Benes, E. Capelli, Cesium and iodine release from fluoride-based molten salt reactor fuel, Phys. Chem. Chem. Phys. 23 (2021) 9512–9523, https://doi.org/10.1039/d0cp05794k.
[19] D. Williams, A. Pinchera, A. Karaoglou, K.H. Chadwick, Thyroid cancer in children living near Chernobyl: Expert Panel report on the consequences of the Chernobyl accident, European, Communities (1993).
[20] J.H. Kim, L.R. Mandell, R. Leeper, Radiation Effects on the Thyroid Gland, Advances in Radiation Biology 14 (1990) 119–156, https://doi.org/10.1016/B978-0-12-035414-6.50009-2.
[21] W.M. Stacey, Nuclear Reactor Physics, Second, WILEY-VCH Verlag GmbH & Co. KGaA, Weinheim, Germany, 2007.
[22] M.V. Malko, T. (Eds.). Manaka, The Chernobyl Reactor: Design Features and Reasons for Accident in Recent Research Activities About the Chernobyl NPP Accident in Belarus, Ukraine and Russia, Kyoto, 2016.
[23] G.L. Fredrickson, M.N. Patterson, D. Vaden, G.G. Galbreth, T.-S. Yoo, J.C. Price, E. J. Flynn, R.N. Searle, History and status of spent fuel treatment at the INL fuel conditioning facility, Prog. Nucl. Energy. 143 (2022) 104037, https://doi.org/10.1016/j.pnucene.2021.104037.
[24] J.J. Laidler, J.E. Battles, W.E. Miller, J.P. Ackerman, E.L. Carls, Development of pyroprocessing technology, Prog. Nucl. Energy. 31 (1997) 131–140, https://doi.org/10.1016/0149-1970(96)00007-8.
[25] I. Johnson, The thermodynamics of pyrochemical processes for liquid metal reactor fuel cycles, J. Nucl. Mater. 154 (1988) 169–180, https://doi.org/10.1016/0022-3115(88)90131-6.
[26] J.P. Ackerman, Chemical basis for pyrochemical reprocessing of nuclear fuel, Ind. Eng. Chem. Res. 30 (1991) 141–145, https://doi.org/10.1021/ie00049a022.
[27] C.W. Bale, E. Bélisle, P. Chartrand, S.A. Decterov, G. Eriksson, A.E. Gheribi, K. Hack, I.-H. Jung, Y.-B. Kang, J. Melançon, A.D. Pelton, S. Petersen, C. Robelin, J. Sangster, P. Spencer, M.-A. Van Ende, Reprint of: FactSage thermochemical software and databases, 2010–2016, Calphad 55 (2016) 1–19, https://doi.org/10.1016/j.calphad.2016.07.004.
[28] E.B. Ferreira, M.L. Lima, E.D. Zanotto, DSC method for determining the liquidus temperature of glass-forming systems, J. Am. Ceram. Soc. 93 (2010) 3757–3763, https://doi.org/10.1111/j.1551-2916.2010.03976.x.
[29] A.S. Pedersen, N. Pryds, S. Linderoth, P.H. Larsen, J. Kjøller, The determination of dynamic and equilibrium solid/liquid transformation data for Sn–Pb using DSC, J. Therm. Anal. Calorim. 64 (2001) 887–894, https://doi.org/10.1023/A:1011506526074.
[30] L. Vegard, Die Konstitution der Mischkristalle und die Raumfüllung der Atome, Zeitschrift Für Phys. 5 (1921) 17–26, https://doi.org/10.1007/BF01349680.
[31] B. Amrani, A. Kazempoor, S. Khosravizadeh, F. El Haj Hassan, H. Akbarzadeh, Theoretical investigations on KCl_xBr_{1-x}, KCl_xI_{1-x} and KBr_xI_{1-x}: A first-principles study, Phys. B Condens. Matter. 403 (2008) 2773–2779, https://doi.org/10.1016/j.physb.2008.02.009.